Re-entry trajectory optimization using pigeon inspired optimization based control profiles ☆

Gangireddy Sushnigdha *, Ashok Joshi

Department of Aerospace Engineering, IIT Bombay, Mumbai, India

Abstract

In this paper, the entry trajectory optimization problem of lifting type re-entry vehicle with path constraints is solved using Pigeon Inspired Optimization (PIO). Entry trajectory optimization problem involves finding the control profiles, bank angle, and angle of attack to guide the vehicle safely to the destination. The proposed approach parametrizes the bank angle to be a linear function of energy while the angle of attack is considered to be a monotonic function of Mach number. Thus, the problem of finding control profiles is transformed into three parameter search problem. The PIO algorithm is used to find the values of these parameters that minimizes the objective function. The terminal heading angle offset is minimized using traditional bank reversal logic. A new approach is proposed in which the bank angle is modulated to eliminate the oscillations observed in the altitude profile of an entry vehicle with a high lift to drag ratio (L/D). A methodology to satisfy the given load factor constraint is also proposed, as an alternative to traditional penalty factor approach used for incorporating path constraints in PIO algorithm. The proposed approach is further validated by considering sub-cases with different load factor limits and bank angle as the only control variable. The angle of attack profile obtained from the previous case is considered as the nominal profile. The proposed trajectory optimization strategy using PIO algorithm is simulated for Common Aero Vehicle with high L/D ratio (CAV-H) with different load factor constraint limits. The results show that the obtained angle of attack profile minimizes the peak heat rate experienced by the vehicle and bank angle modulation eliminates the oscillations in the altitude profile as well as makes the entry trajectory satisfy the load factor constraint.
© 2018 COSPAR. Published by Elsevier Ltd. All rights reserved.

Keywords: Pigeon inspired optimization; Entry trajectory optimization; Meta-heuristic algorithms; Re-entry

1. Introduction

The curiosity towards space exploration has increased over the years which has led to the development of many spacecraft and launch vehicles. Some of these vehicles are required to return Earth safely either to bring back the astronauts or to facilitate their reuse. Two main aspects of such vehicles are; the ascent mission and the re-entry mission. The re-entry phase of re-entry mission is very crucial for any spacecraft that is returning from space to the Earth. In this phase, the vehicle is unpowered and therefore, the trajectory is governed only by gravity and aerodynamic forces. The control over the entry trajectory is obtained by modulating the bank angle and/or angle of attack. These control commands are to be determined by the guidance module. Guidance algorithms usually employ a trajectory planner to generate a feasible trajectory that satisfies the predefined heat rate, and g-load limits and a tracker to follow the planned trajectory. The present work will focus on developing a trajectory planning approach which generates constrained entry trajectories.

Re-entry trajectory planning problem is regarded as an optimal control problem. Optimal control tools can handle path and terminal constraints while minimizing or maximizing a specified performance index. These optimal control problems are solved using numerical methods which are divided into two major classes: indirect and direct methods. Indirect methods are based on the Pontryagin minimum principle which leads to two-point boundary value problem as given in Pontryagin and Boltyanskii (1987). Direct methods involve discretizing control time histories and/or state variable time history, thereby transforming the optimal control problem to a nonlinear programming problem (NLP) Betts (2001). Pseudospectral methods that fall under the category of direct method are being used extensively for solving trajectory optimization problems. Bailing and Qun (2011) have implemented a Legendre pseudospectral method for entry trajectory optimization. Cai et al. (2015) have applied the Chebyshev pseudospectral method for generating entry trajectories. However, pseudospectral methods have tuning issues such as selection of the basis functions and the number of collocation points. Moreover, these algorithms are also sensitive to initial guess values of the control and state variables.

The meta-heuristic algorithms that mimic natural phenomena fall under the category of direct methods. These algorithms are simple and involve derivative free approach of arriving at the optimal solution. Genetic Algorithm (GA), Particle Swarm Optimization (PSO), Simulated annealing (SA) are some of the heuristic algorithms. Some of the latest developments of meta-heuristic algorithms are Whale optimization, Grasshopper optimization. They are used for solving optimization problems in various domains Yu et al. (2017) and Wu et al. (2017, 2018). In recent times, Duan has proposed a meta-heuristic algorithm that mimics the homing behavior of pigeons in Duan and Qjao (2014). Pigeons have special ability to sense the magnetic field of Earth and measure the altitude of the Sun. This feature is termed as map and compass operator. They also have the ability to identify the landmarks, which is termed as a landmark operator. These features of PIO algorithm makes it different from other meta-heuristic approaches and has potential to solve optimization problems. PIO algorithm is also modified to address different scenarios such as target detection task for Unmanned Aerial Vehicles in Li and Duan (2014), path planning of uninhabited combat aerial vehicle in Zhang and Duan (2017), image restoration in Duan and Wang (2016), designing control parameters in Xue and Duan (2017) and Deng and Duan (2016) and for solving multi-objective optimization problems in Qiu and Duan (2015). This paper utilizes basic PIO algorithm to generate feasible entry trajectories.

Optimal trajectories of a spacecraft are generated using PSO algorithm in Rahimi et al. (2013). PSO and PIO algorithms are used to generate entry trajectories for hypersonic gliding vehicle by Zhao and Zhou (2015a,b). Zhao and Zhou (2015a,b) have considered the control formulation that requires finding multiple parameters to get the complete control profile. However, they have considered only bank angle as the control variable with a nominal angle of attack profile and demonstrated few entry cases which involve one or two bank reversals and cover shorter ranges. The constraints on load factor are implemented using penalty factor approach. Moreover, the obtained entry trajectories exhibit oscillations which increase heat rate, and g-loads. Sushnigdha and Joshi (2017) have used PIO algorithm to find the bank angle profile for generating the entry trajectory of CAV-H vehicle. It is observed that the convergence of PIO is faster than PSO and Gravitational Search Algorithms (GSA) when the dimension of the problem is one. It is to be noted that the entry trajectory obtained using PIO in Sushnigdha and Joshi (2017) also has undesirable oscillations. This issue can be solved by incorporating equilibrium glide condition.

This paper presents a constrained entry trajectory optimization problem which is solved using PIO, to find the control histories which are used to generate the entry trajectories. In the first case, the PIO algorithm is used to find the bank angle and angle of attack control profiles. These control variables are parametrized and the problem is formulated as three parameter search problem. PIO algorithm is used to find these three parameters that minimize the objective function which consists of peak heat rate and terminal errors. A new scheme that modulates bank angle to further satisfy equilibrium glide condition and load factor constraints is incorporated in the problem formulation. By treating the angle of attack profile obtained from the first case as the nominal profile, few sub-cases are considered. In these sub-cases, the trajectory optimization problem is converted into a single parameter search problem of finding the bank angle for different load factor constraints. Further, few cases and sub-cases to verify the robustness of the proposed methodology in the presence of dispersions in the initial entry conditions, parameters are considered and applicability of the proposed strategy for different entry missions is also tested.

This paper is organized as follows. In Section 2, details of the considered re-entry vehicle, its equations of motion, gravity, atmosphere models, path and terminal constraints are discussed. The entry trajectory optimization problem, parametrization of control variables and objective functions are defined in Section 3. Section 4 explains the PIO algorithm with QEGC and path constraints handling mechanism. In Section 5, simulation results are discussed. Section 6 concludes the paper.

2. Mathematical model and details of re-entry vehicle

This section gives an introduction to the re-entry vehicle CAV-H which is used for the simulations and describes the equations of motion, gravity model, atmospheric model, terminal and path constraints.

2.1. CAV-H

The Common Aero Vehicle (CAV) is a concept which describes a space re-entry aeroshell launched into space on a suitable vehicle. After which, CAV survives atmospheric re-entry, reduces its speed to low Mach numbers and dispenses a cargo, payload or weapon in the atmosphere of the Earth (Phillips, 2003). There are two types of common aero vehicles. In this paper, CAV-H is used for simulations. The mass of the vehicle is 907.2 kg and the surface area is 0.4839 m². The maximum L/D ratio for the vehicle is 3.5.

2.2. Equations of motion

By considering the re-entry vehicle to be a point mass, the equations of motion of the vehicle gliding over a spherical, rotating Earth in terms of nondimensional variables are given as follows (Lu, 2014)

$$\dot{r} = V \sin \gamma \tag{1}$$

$$\dot{\theta} = \frac{V \cos \gamma \sin \psi}{r \cos \phi} \tag{2}$$

$$\dot{\phi} = \frac{V \cos \gamma \cos \psi}{r} \tag{3}$$

$$\dot{s} = -V \cos \gamma / r \tag{4}$$

$$\dot{V} = -D - \left(\frac{\sin \gamma}{r^2}\right) + \Omega^2 r \cos \phi (\sin \gamma \cos \phi - \cos \gamma \sin \phi \cos \psi) \tag{5}$$

$$\dot{\gamma} = \frac{1}{V} \left[L \cos \sigma + \left(V^2 - \frac{1}{r}\right)\left(\frac{\cos \gamma}{r}\right) + 2\Omega V \cos \phi \sin \psi \right.$$
$$\left. + \Omega^2 r \cos \phi (\cos \gamma \cos \phi + \sin \gamma \cos \psi \sin \phi) \right] \tag{6}$$

$$\dot{\psi} = \frac{1}{V} \left[\frac{L \sin \sigma}{\cos \gamma} + \frac{V^2}{r} \cos \gamma \sin \psi \tan \phi \right.$$
$$\left. - 2\Omega V (\tan \gamma \cos \psi \cos \phi - \sin \phi) + \frac{\Omega^2 r}{\cos \gamma} \sin \psi \sin \phi \cos \phi \right] \tag{7}$$

Eqs. (1)–(4) are kinematic equations and Eqs. (5)–(7) are dynamic equations. The derivatives in the above equations of motion are with respect to dimensionless time τ in the above mentioned equations of motion. The dimensional time t is calculated using $t = t_{scale}\tau$, where $t_{scale} = \sqrt{\frac{R_0}{g_0}}$. The nondimensional distance from the Earth center to the point mass O that is normalized by the radius of the Earth $R_0 = 6378.135$ km is denoted by r. The Earth-relative velocity V is normalized by $V_{scale} = \sqrt{R_0 g_0}$, where g_0 is the acceleration due to gravity on the surface of the Earth. θ and ϕ are the longitude and latitude, the flight-path angle γ is positive when V is above the horizontal plane. ψ is the heading angle of the velocity vector, measured clockwise in the local horizontal plane from the
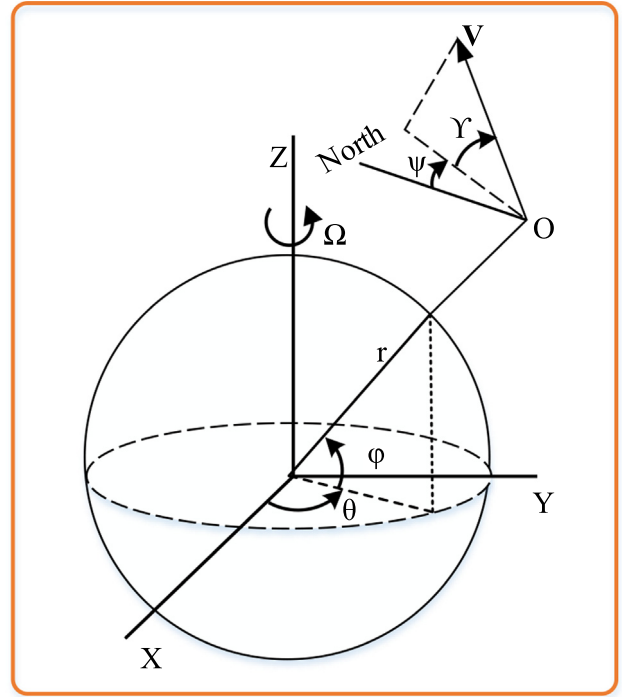

Fig. 1. Nomenclature used in equations of motion.

north as shown in Fig. 1. The range-to-go s (in radians, normalized by R_0) is defined on the surface of the spherical Earth along the great circle connecting the current location of the vehicle and the site of the final destination Lu (2014). Bank angle σ is defined as the clockwise positive rotation of the lift vector about the velocity vector. Ω is the dimensionless angular velocity of the Earth. The nondimensional aerodynamic lift, L and drag, D accelerations are normalized with $g_0 = 9.8$ m/s² and are defined as

$$L = \frac{1}{2mg_0} \rho V^2 C_L S_{ref} \tag{8}$$

$$D = \frac{1}{2mg_0} \rho V^2 C_D S_{ref} \tag{9}$$

where m is the mass of the vehicle, the surface area of the wing is S_{ref}, and ρ is the atmospheric density. The aerodynamic lift coefficient C_L and drag coefficient C_D are functions of the angle of attack and Mach number. The aerodynamic coefficient details of CAV-H are in Phillips (2003).

2.3. Choice of independent variable and calculation of final time of flight t_f

The entry trajectory optimization problem is solved by considering an energy like variable e as the independent variable. It is defined as negative of the specific mechanical energy used in orbital mechanics as mentioned in Lu (2014).

$$e = \frac{\mu}{r} - \frac{V^2}{2} \tag{10}$$

$$\dot{e} = DV \tag{11}$$

where μ is a gravitational parameter of the Earth, whose normalized value is 1. e is a monotonically increasing variable as seen in Eq. (11) and is also a function of radial distance and velocity. The choice of e as an independent variable reduces the terminal conditions on r and V to a single constraint. The order of the system is also reduced by eliminating Eq. (5) and velocity V at any instant is calculated using Eq. (10). The above described equations of motion are rewritten considering e as independent variable by using Eq. (11) as $dr/de = \dot{r}/\dot{e}$, etc. The equations of motion are integrated from initial energy e_0 to final energy e_f. Energy at entry interface e_0 and energy at the end of re-entry phase e_f are calculated using the initial and desired values of radial distances r_0, r^* and velocities V_0, V^* respectively. The final time of flight t_f is obtained as part of the solution process by including $\frac{d\tau}{de}$ in the equations of motion.

2.4. Gravity model

The acceleration due to gravity of the vehicle at a radial distance r from the centre of Earth is given by Eq. (12)

$$g = \frac{\mu}{r^2} \tag{12}$$

The nondimensional value of gravitational parameter μ is 1. This gravity model is considered in the equations of motion.

2.5. Atmosphere

The U.S. Standard Atmosphere, 1976 is used to model the atmosphere Anon (1976). The atmospheric density at an altitude is obtained using Eq. (13)

$$\rho = \rho_0 e^{-\beta(r-1))} \tag{13}$$

where ρ_0 is the density on the surface of the Earth, $\rho_0 = 1.225 \text{ kg/m}^3$ and $\beta = 920$ is nondimensional scale height which is normalized with the radius of the Earth.

2.6. Path constraints

The vehicle has to travel within the entry corridor formed by the upper limits of specified heat rate $\dot{Q}_{max}$, load factor a_{max} and dynamic pressure q_{max} in the re-entry phase. These constraints are termed as path constraints and given by the following equations.

$$\dot{Q} = 9.4369 \times 10^{-5} \sqrt{\rho} V^{3.15} V_{scale}^{3.15} \leqslant \dot{Q}_{max} \tag{14}$$

$$a = \sqrt{L^2 + D^2} \leqslant a_{max} \tag{15}$$

$$q = \frac{\rho V^2 V_{scale}^2}{2} \leqslant q_{max} \tag{16}$$

These path constraints are to be strictly satisfied. Equilibrium glide constraint given in Eq. (17) is regarded as the soft constraint. Equilibrium glide refers to the case where the aerodynamic lift force balances the gravitational and centrifugal forces. This equation is obtained by making the derivative of flight-path angle zero and neglecting the Earth rotation terms.

$$L\cos\sigma = (1/r^2) - (V^2/r) \tag{17}$$

During the equilibrium glide condition, flight-path angle should ideally be constant, however, it varies slowly. Hence, it is termed as Quasi Equilibrium Glide condition (QEGC) in Lu (2006). Entry vehicles with high lift to drag ratio exhibit oscillations in their altitude profiles which lead to high heat rate and g-loads. These oscillations can be eliminated when the vehicle satisfies QEGC constraint.

2.6.1. Entry corridor

All the path constraints given by Eqs. (14)–(17) are converted to limits on altitude. By using the equations given below, these constraints are represented in altitude-velocity space as shown in Fig. 2.

$$r \geqslant r_Q = 1 + \frac{1}{\beta} \ln \left(\frac{1.225 k_q^2 V^{6.3} V_{scale}^{6.3}}{\dot{Q}_{max}^2} \right) \tag{18}$$

$$r \geqslant r_a = 1 + \frac{1}{\beta} \ln \left(\frac{1.225 V^2 V_{scale}^2 S_{ref} C_D \sqrt{L^2 + D^2}}{2 a_{max} m D g_0} \right) \tag{19}$$

$$r \geqslant r_q = 1 + \frac{1}{\beta} \ln \left(\frac{1.225 V^2 V_{scale}^2}{2 q_{max}} \right) \tag{20}$$

$$r \leqslant r_{eq} = 1 + \frac{1}{\beta} \log \left(\frac{V_{scale}^2 V^2 \rho_0 S_{ref} C_L}{2 m g_0 (1 - V^2)} \right) \tag{21}$$

At any given velocity, the vehicle should fly at altitudes higher than $\max[r_Q, r_q, r_a]$, in order to satisfy the above mentioned path constraints. These altitudes form the lower bound in the altitude-velocity space. The equilibrium glide
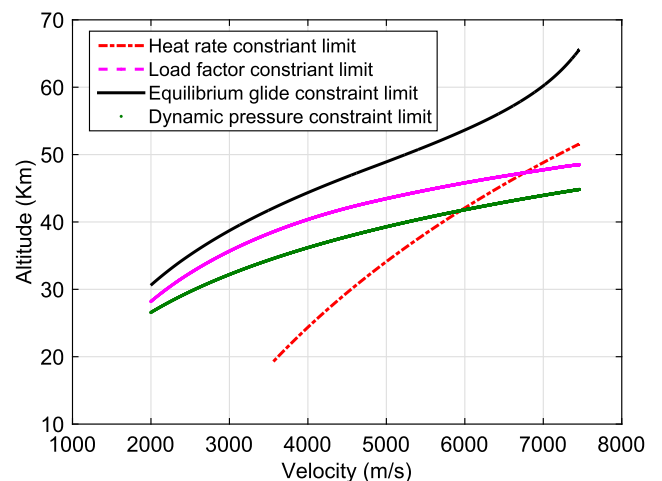

Fig. 2. Entry corridor formed by path constraints.

constraint forms the upper bound on the altitude. It is seen that heat rate constraint is active in the initial descent phase of the entry flight and subsequently load factor and dynamic pressure constraints become active. Dynamic pressure constraint can be satisfied implicitly by satisfying the load factor constraint limit as seen in Fig. 2 in some cases. In such cases, heat rate and load factor constraints only form the path constraints. The proposed strategies to satisfy QEGC and load factor constraints make use of the above mentioned constraint limits on altitude in Section 5.

2.7. Terminal constraints

At the end of entry phase, the vehicle needs to achieve a radial distance r^*, range-to-go s^* and velocity V^* as per the requirement of the Terminal Area Energy Management (TAEM) phase. The heading angle offset $\Delta\psi_f$ at the end of entry phase should be less than the desired heading angle offset $\Delta\psi^*$ as given in Eq. (22).

$$\left|\Delta\psi_f\right| \leqslant \Delta\psi^* \tag{22}$$

3. Entry trajectory optimization problem

Trajectory optimization of entry vehicles involves finding the control profiles such that the resulting entry trajectory satisfies the path and terminal conditions. In cases 1, 2, and 3 both bank angle and angle of attack are considered to be the control variables. To solve this optimal control problem, bank angle is parametrized with respect to energy e and angle of attack is considered to be a monotonic function of Mach number, as given below.

3.1. Angle of attack parametrization

The angle of attack profile is considered to be a monotonic function of Mach number M as shown in Fig. 3. A constant angle of attack is considered when the vehicle is at high Mach numbers. After Mach number $M < m_{pio}$,
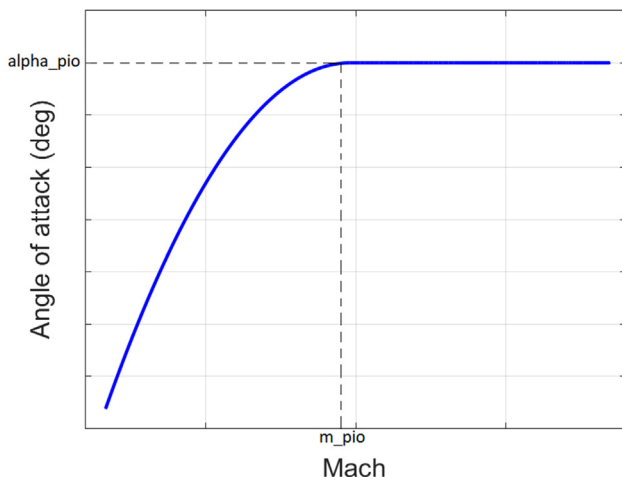

Fig. 3. Monotonic angle of attack profile.

angle of attack is monotonically decreasing with a chosen slope of 0.1 as defined by Eq. (23).

$$\alpha(M) = \begin{cases} \alpha_{pio}, & M \geqslant m_{pio} \\ \alpha_{pio} - 0.1\left(M - m_{pio}\right)^2, & M < m_{pio} \end{cases} \tag{23}$$

In Eq. (23), the Mach number m_{pio} and the angle of attack α_{pio} are the parameters to be found in order to get the complete angle of attack profile.

3.2. Bank angle parametrization

The control variable, bank angle is considered to be a linear function of current energy e, based on piecewise linear approximation. Its magnitude is calculated from Eq. (24)

$$\left|\sigma(e)\right| = \sigma_0 + \frac{e - e_0}{e_f - e_0}\left(\sigma_f - \sigma_0\right) \tag{24}$$

where e_0 and e_f are energies at entry interface and terminal points respectively. $\sigma_0 \geqslant 0$ is the parameter to be found that minimizes the given objective function. σ_f is the predefined terminal bank angle and $\sigma_f = 60°$ is chosen for the simulations. The sign of bank angle is obtained from a bank reversal logic as described by in Shen and Lu (2004). This bank reversal logic is used to reduce the terminal heading error offset.

3.3. Objective function

The objective function for PIO based trajectory optimization problem is defined here. In the first three cases, the decision variables to be found are bank angle σ_0, angle of attack α_{pio} and Mach number m_{pio}. In the remaining sub-cases, the decision variable to be found is one i.e. bank angle σ_0. The angle of attack profiles obtained in the first three cases are considered to be the nominal angle of attack profiles for corresponding sub-cases. The objective functions for different cases and sub-cases are given below:

3.3.1. Objective function for different cases
Trajectory optimization problem is stated as;
Find the decision variables σ_0, m_{pio} and α_{pio} that minimize peak heat rate and terminal constraint errors as described in J, given below

$$\begin{aligned} Min J = &\frac{max(\dot{Q})}{10^5} + \frac{\left|s(e_f) - s^*\right| \times R_0}{10^3} \\ &+ \frac{\left|r(e_f) - r^*\right| \times R_0}{1000} + \frac{\left|V(e_f) - V^*\right| \times V_{scale}}{100} \end{aligned} \tag{25}$$

subject to
Equations of motion, quasi equilibrium glide constraint given by Eq. (17) and load factor constraint in Eq. (15).
In the objective function, "$*$" indicates the desired terminal states as defined by the TAEM phase. The terms in the objective function are dimensional, range-to-go term is in m, radial distance term is in km and velocity in m/s and

the terms are multiplied with some weights to bring them to the same order of magnitude as given in Eq. (25).

3.3.2. Objective function for sub-cases

The angle of attack profile obtained in the first case is considered to be the nominal profile and only bank angle variable σ_0 is to be found. Each term in Eq. (26) is dimensional as described in the case 1. Minimum peak heat rate depends on the angle of attack profile. As the angle of attack profile is same as the previous cases, the term corresponding to peak heat rate is eliminated in the current objective function, which is;

$$MinJ = \frac{|s(e_f) - s^*| \times R_0}{10^3} + \frac{|r(e_f) - r^*| \times R_0}{1000}$$
$$+ \frac{|V(e_f) - V^*| \times V_{scale}}{100} \tag{26}$$

subject to

Equations of motion, quasi equilibrium glide constraint given by Eq. (17) and load factor constraint in Eq. (15).

4. Pigeon inspired optimization

Pigeons have special ability to locate themselves relative to their destination by being able to sense the magnetic field of the Earth. They have the ability to adjust their flying direction using altitude of the Sun. They also have the ability to recognize landmarks and can fly directly towards the destination. This PIO algorithm mimics the homing behavior of pigeons and the features of pigeons are classified as map and compass operator, and landmark operator. It is observed that pigeons use map and compass operator during their initial phase of the journey and then use landmarks to reach the destination. Details of these operators are given below.

4.1. Map and compass operator

Initialize the total population of the pigeons N. Set the maximum number of iterations k_{max} and define the dimension D of the problem based on the number of unknown variables to be found. Specify the search range for each dimension. In the first iteration, initial set of pigeons are randomly generated in the given search range. The position of the pigeon i is given by Eq. (27).

$$X_i = [x_{i1}, x_{i2}, \ldots, x_{iD}] \quad where \; i = 1, 2, 3 \ldots N \tag{27}$$

The velocity of the pigeon i is given by Eq. (28).

$$V_i = [v_{i1}, v_{i2}, \ldots, v_{iD}] \quad where \; i = 1, 2, 3 \ldots N \tag{28}$$

where x_{iD} and v_{iD} are the position and velocity components of each dimension D. Each pigeons position vector X_i represents a possible solution and corresponds to an objective function. The position and velocities of the pigeons are updated in each iteration k as per the following update logic

$$V_i(k) = V_i(k-1).e^{-Rk} + rand.(G(k-1) - X_i(k-1)) \tag{29}$$

$$X_i(k) = X_i(k-1) + V_i(k) \tag{30}$$

where $G(k-1)$ is the best position of the pigeon corresponding to the minimum objective function achieved till the current iteration. The random number $rand$ is in the range $[0, 1]$, which helps in exploring the search space. R is the map and compass operator. In this operator, all the pigeons adjust their position and try to follow the pigeon that corresponds to the best objective function value i.e. minimum objective function value for a minimization problem. The term $V_i(k-1).e^{-Rk}$ gives the pigeons former flying direction. The influence of previous velocity $V_i(k-1)$ in the current updating step is governed by the term e^{-Rk}. With the increase in the number of iterations, the influence of $V_i(k-1)$ in the current updating step decreases, leading to greater exploitation and faster convergence towards the best solution.

4.2. Landmark operator

Pigeons shift their operator to landmark operator as they approach their destination. Few pigeons that can identify the landmarks fly directly to their destinations while the remaining pigeons follow them to reach the destination.

The iteration number k_c which is less than k_{max}, indicates the shift in the operator. The landmark operator is initiated when the current iteration k becomes equal to k_c. k_c is chosen to be 75% of k_{max} as given in Duan and Qiao (2014). In this operator, half of the pigeons with positions close to $G(k-1)$ are selected. The centre of these pigeons is found using Eq. (31).

$$X_c(k) = \frac{\sum_{N_p(k)} X_i(k-1).fitness(X_i(k-1))}{N_p(k) \sum_{N_p(k)} fitness(X_i(k-1))} \tag{31}$$

where $fitness()$ is the objective function value corresponding to the given pigeons position and N_p is the current reduced population as given below

$$N_p(k) = \frac{N_p(k-1)}{2} \tag{32}$$

The positions of the pigeons is updated using $X_c(k)$ as follows

$$X_i(k) = X_i(k-1) + rand.(X_c(k) - X_i(k-1)) \tag{33}$$

In this operator, the pigeons that are unfamiliar with the landmarks adjust their positions and follow the center of the pigeons that are familiar with the landmarks. Towards the end of iterations, pigeon corresponding to minimum objective function value will be the pigeon with the best position.

4.3. Method to incorporate quasi equilibrium glide constraint

This section utilizes the slope of altitude limit corresponding to QEGC shown in Fig. 2, to modulate the bank angle and to make the entry trajectory satisfy QEGC constraint. Quasi Equilibrium glide condition corresponds to $\dot{\gamma} = 0$ in Eq. (6) and is obtained by ignoring the terms related to rotation of the Earth as given by Eq. (34).

$$L \cos \sigma + \left(V^2 - \frac{1}{r}\right)\left(\frac{\cos \gamma}{r}\right) = 0 \tag{34}$$

In the above equation, σ is constant and is chosen to be 0 and $r \approx 1$ and $\gamma \approx 0$. Then the resulting equation is

$$L + \left(V^2 - 1\right) = 0 \tag{35}$$

Note that the above equation has nondimensional quantities. By substituting lift acceleration given by Eq. (8) in the above equation gives

$$\frac{\rho V^2 C_L S_{ref}}{2mg_0} + V^2 - 1 = 0 \tag{36}$$

Atmospheric density ρ is an exponential function of radial distance r given by Eq. (13). This expression of density is substituted in Eq. (36), results in

$$\frac{\rho_0 e^{-\beta(r-1)} V^2 C_L S_{ref}}{2mg_0} + V^2 - 1 = 0 \tag{37}$$

By using the above equation, the relationship between altitude and velocity can be derived as given below

$$r_{eq} = 1 + \frac{1}{\beta} \log\left(\frac{V_{scale}^2 V^2 \rho_0 S_{ref} C_L}{2mg_0(1 - V^2)}\right) \tag{38}$$

Eq. (38), gives the altitude required to satisfy equilibrium glide condition at any given velocity. On differentiating the above equation with respect to velocity results in Eq. (39)

$$\frac{dr_{eq}}{dV} = \frac{1}{\beta V^2(1 - V^2)} \tag{39}$$

Eqs. (1) and (5) from the equations of motion are used to equate the above Eq. (39) as given below

$$\frac{V \sin\gamma}{-D - (\sin \gamma / r^2)} = \frac{1}{\beta V^2(1 - V^2)} \tag{40}$$

From the above Eq. (40), flight-path angle required to fly the vehicle at equilibrium glide condition is obtained as

$$\sin\gamma_{QEGC} = \frac{-D}{\beta V^3(1 - V^2) + (1/r^2)} \tag{41}$$

The above expression for γ_{QEGC} can be used to find the altitude rate required to fly the vehicle at QEGC. The altitude variation with respect to energy to fly at QEGC is

$$\frac{dr_{QEGC}}{de} = \frac{\sin\gamma_{QEGC}}{D} \tag{42}$$

The current variation of altitude with respect to energy is given by

$$\frac{dr}{de} = \frac{\sin\gamma}{D} \tag{43}$$

The vertical component of lift force is modulated by using the altitude compensation term $k\left(\frac{dr}{de} - \frac{dr_{QEGC}}{de}\right)$, given in Eq. (44).

$$L \cos \sigma_{cmd} = L \cos \sigma_{base} - k_1\left(\frac{dr}{de} - \frac{dr_{QEGC}}{de}\right) \tag{44}$$

where σ_{base} is the bank angle at current energy obtained using Eq. (24). $k_1 > 0$ is the gain which is scheduled as a linear function of velocity. Bank angle σ_{cmd} is used to integrate the equations of motion and the objective function is evaluated. This bank angle σ_{cmd} eliminates the oscillations observed when QEGC is not satisfied. In cases which demand constraint on load factor or dynamic pressure to be satisfied, the σ_{cmd} is further modified to satisfy the required constraints and σ_{cmd} in Eq. (44) is referred to as σ_{QEGC}.

4.4. Incorporating constraints on load factor

The constraints on load factor and dynamic pressure are converted to limits on altitude as given in Eqs. (19) and (20) respectively. The slope of altitude-velocity curve formed due to constraint on load factor is given below

$$\frac{dr_a}{dV} = \frac{2}{\beta V} \tag{45}$$

Using Eqs. (1) and (5) from equations of motion and equating it with Eq. (45) results in the equation given below

$$\frac{V \sin\gamma}{-D - (\sin \gamma / r^2)} = \frac{2}{\beta V} \tag{46}$$

From the above Eq. (46), flight-path angle required to satisfy the constraint on load factor is obtained as

$$\sin\gamma_a = \frac{-2D}{\beta(V^2 + (2/\beta r^2))} \tag{47}$$

This flight-path angle is used to obtain the altitude variation with respect to energy to satisfy load factor constraints.

$$\frac{dr_a}{de} = \frac{\sin\gamma_a}{D} \tag{48}$$

The current variation of altitude with respect to energy is given by

$$\frac{dr}{de} = \frac{\sin\gamma}{D} \tag{49}$$

To follow QEGC along with load factor constraint, The bank angle σ_{cmd} can be obtained using Eq. (50)

$$L \cos \sigma_{cmd} = L \cos \sigma_{QEGC} - k_2\left(\frac{dr}{de} - \frac{dr_a}{de}\right) \tag{50}$$

where σ_{QEGC} is the bank angle at the current energy obtained using Eq. (44). $k_2 = 70$ is a constant gain used
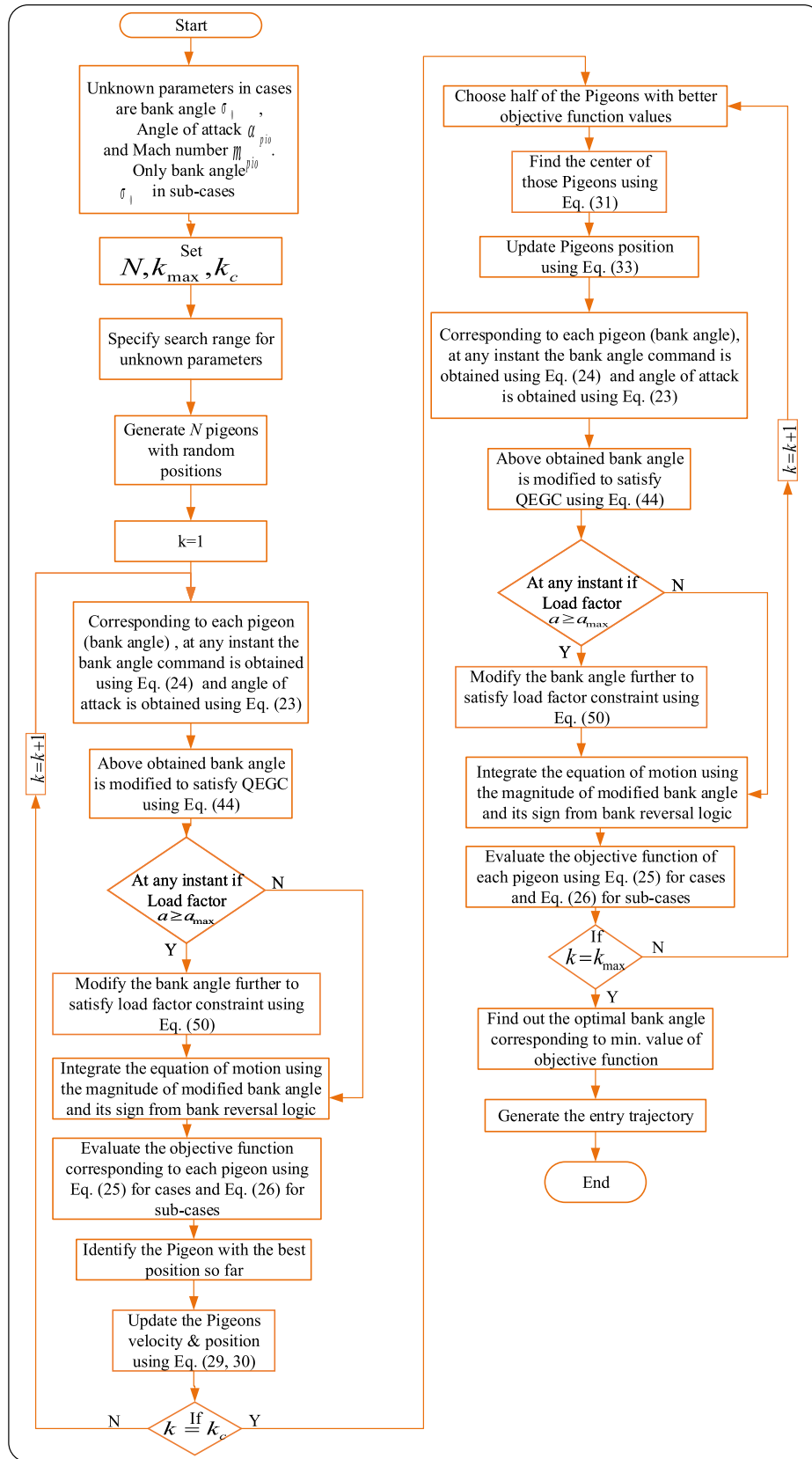
Start

Unknown parameters in cases are bank angle σ_{pio}, Angle of attack α_{pio} and Mach number m_{pio}. Only bank angle σ_{pio} in sub-cases

Set $N, k_{\max}, k_c$

Specify search range for unknown parameters

Generate N pigeons with random positions

k=1

Corresponding to each pigeon (bank angle), at any instant the bank angle command is obtained using Eq. (24) and angle of attack is obtained using Eq. (23)

Above obtained bank angle is modified to satisfy QEGC using Eq. (44)

At any instant if Load factor $a \geq a_{\max}$

N

Y

Modify the bank angle further to satisfy load factor constraint using Eq. (50)

Integrate the equation of motion using the magnitude of modified bank angle and its sign from bank reversal logic

Evaluate the objective function corresponding to each pigeon using Eq. (25) for cases and Eq. (26) for sub-cases

Identify the Pigeon with the best position so far

Update the Pigeons velocity & position using Eq. (29, 30)

If $k = k_c$ N   Y

$k=k+1$

Choose half of the Pigeons with better objective function values

Find the center of those Pigeons using Eq. (31)

Update Pigeons position using Eq. (33)

Corresponding to each pigeon (bank angle), at any instant the bank angle command is obtained using Eq. (24) and angle of attack is obtained using Eq. (23)

Above obtained bank angle is modified to satisfy QEGC using Eq. (44)

At any instant if Load factor $a \geq a_{\max}$ N

Y

Modify the bank angle further to satisfy load factor constraint using Eq. (50)

Integrate the equation of motion using the magnitude of modified bank angle and its sign from bank reversal logic

Evaluate the objective function of each pigeon using Eq. (25) for cases and Eq. (26) for sub-cases

If $k = k_{\max}$ N

Y

$k=k+1$

Find out the optimal bank angle corresponding to min. value of objective function

Generate the entry trajectory

End

Fig. 4. PIO algorithm with QEGC and load factor constraints.

Table 1
Initial entry conditions.

Cases	r_0 (km)	V_0 (m/s)	θ_0 (deg)	ϕ_0 (deg)	γ_0 (deg)	ψ_0 (deg)	s_0 (km)
Case 1	121.52	7400	−72.42	38.99	−1	35	11,112
Case 2	123.74	7369.7	−72.42	38.99	−1.2	37	11,112
Case 3	119.27	7430.4	−72.42	38.99	−0.8	33	11,112

Table 2
Final conditions to be achieved Lu (2014).

r^* (km)	V^* (m/s)	s^* (km)	$\Delta\psi^* \leqslant$ (deg)
28	2000	92.6	±10

Table 3
Parameters used in PIO for solving cases and sub-cases.

Cases\Parameters	N	D	k_{max}	k_c	R
Cases	40	3	25	15	0.2
Sub-cases	10	1	25	15	0.2

Table 4
Parameters used in PSO algorithm for solving cases.

Parameters	Values
Population size	40
Acceleration constants (c_1 and c_2)	1.4, 2.6
Inertia constants (w_{max} and w_{min})	1, 0.4
Maximum iterations	25

in the above equation. This Eq. (50) is used only when the load factor constraint is violated and this bank angle σ_{cmd} is used to integrate the equations of motion. If the load factor constraint is not violated, bank angle obtained from Eq. (44) is only used to integrate equations of motion without any further modifications. The proposed methodology for incorporating QEGC and load factor constraints is included in the prediction process of PIO algorithm so that the obtained entry trajectory satisfies the path constraints.

4.5. PIO algorithm with QEGC and load factor constraint

The path constraints, QEGC and load factor constraints are included as part of the prediction process in the PIO algorithm. In each iteration, each pigeon represents a bank angle σ_0. By using each σ_0, bank angle at each instant is obtained using Eq. (24). This instantaneous bank angle is taken as σ_{base} and is modified to satisfy the QEGC using Eq. (44). The commanded bank angle that satisfies QEGC is obtained as σ_{cmd} from Eq. (44). Using this commanded bank angle with its sign from bank reversal logic, the equations of motion are integrated from e_0 to e_f. At any instant if the load factor constraint is violated, bank angle σ_{cmd} obtained from Eq. (44) is referred to as σ_{QEGC} and is modified using Eq. (50). The bank angle σ_{cmd} obtained using Eq. (50) satisfies both QEGC and load factor constraints. On using this bank angle command with its sign from bank reversal logic, equations of motion are integrated and the

objective function is evaluated using Eq. (25) or Eq. (26) depending on the considered case. At the end of each iteration of PIO algorithm, pigeon with the best objective function is obtained. Based on the path constraint limits a_{max}, q_{max} considered for the simulations, it is seen that if the vehicle travels at altitudes higher than the altitude limit formed by load factor constraint, vehicle automatically satisfies the constraint on dynamic pressure. In cases where the dynamic pressure constraint at any instant is violated, the same σ_{cmd} obtained from Eq. (50) is to be used. This is because the slope dr/dV of load factor and dynamic pressure curves in altitude-velocity space are the same. This can be verified by taking derivative of r_q in Eq. (20) with respective velocity V. The flowchart of PIO algorithm for solving current problem with QEGC and load factor constraint is given in Fig. 4. The proposed schemes for incorporating QEGC and load factor constraints can also be used as part of guidance algorithms like predictor-corrector.

5. Simulation results

The simulation results are demonstrated for CAV-H vehicle. PIO algorithm finds the entry trajectory that satisfies heat rate, load factor, QEGC and terminal constraints. To test the robustness of the proposed scheme of entry trajectory optimization, three cases are considered with dispersions in the initial conditions and load factor constraint limit as $a_{max} = 1.65$ g. In these cases, the dimension of the problem is three. The angle of attack profiles obtained in these cases are considered as the nominal control variable for corresponding each sub-case with different load factor constraint limits a_{max}. The dimension of the problem in these sub-cases is one. Parametric dispersions are also introduced in the sub-cases 4, 5, and cases S1–S5. To test the applicability of the proposed approach, 5 missions with different latitude and longitudes of entry interface and destinations are considered with $a_{max} = 1.65$ g. Simulation results show that the entry trajectories satisfy and fly at the specified upper bounds on load factors. The initial conditions used for all the cases are in Table 1 and the desired terminal conditions are in Table 2. The parameters required for simulating PIO algorithm for the considered cases and sub-cases are given in Table 3. In PIO algorithm, the range of search space for σ_0 is given as $|\sigma_{min}| = 0°$ and $|\sigma_{max}| = 89°$, for angle of attack is $\alpha_{min} = 10°$ and $\alpha_{max} = 20°$ and for Mach number is $M_{min} = 12$ and $M_{max} = 18$. The CAV-H vehicle has maximum L/D at 10° angle of attack according to Phillips (2003) and has aerodynamic control sufficient to maintain angle of attack control

Table 5
Control parameters corresponding to the best objective function obtained using PIO and PSO for case 1, 2 and 3.

Case	Algorithm	σ_0 (deg)	m_{pio}	α_{pio} (deg)	Iterations	J
Case 1	PIO	59.93	14.8	20	11	38.56
	PSO	59.761	14.837	20	24	38.67
Case 2	PIO	56.1050	14.8	20	11	40.3231
	PSO	55.8592	14.76	20	17	40.4149
Case 3	PIO	64.1870	14.801	20	14	36.9068
	PSO	64.1920	14.7347	20	20	36.9920

up to 20°. Therefore, the range of angle of attack in PIO algorithm is taken to be between 10° and 20°. The limits on bank angle magnitude are taken according to Zhao and Zhou (2015a). Upper bound on dynamic pressure $q_{max} = 53,000$ N/m^2. The performance of PIO is compared with Particle Swarm Optimization (PSO). The parameters corresponding to PSO algorithm are given in Table 4. The range of search space and path constraints are same as that of PIO algorithm.

The values of unknown parameters corresponding to the best objective value J obtained using PIO and PSO in cases 1, 2 and 3 are given in Table 5. The performance of PIO over PSO algorithm is shown in Fig. 5. It can be seen that PIO algorithm converges faster than PSO algorithm to the minimum objective function value. Each case is implemented 10 times using PIO and PSO algorithms. The statistical performance comparison of both the algorithms is carried out as shown in Table 6. For all the three cases, the mean and standard deviation of the best objective function value is less in PIO algorithm than PSO algorithm. The mean μ and standard deviation σ of iterations taken to reach minimum objective function value are less in PIO algorithm than PSO algorithm. Therefore, it can be concluded that the performance of PIO is better than PSO.
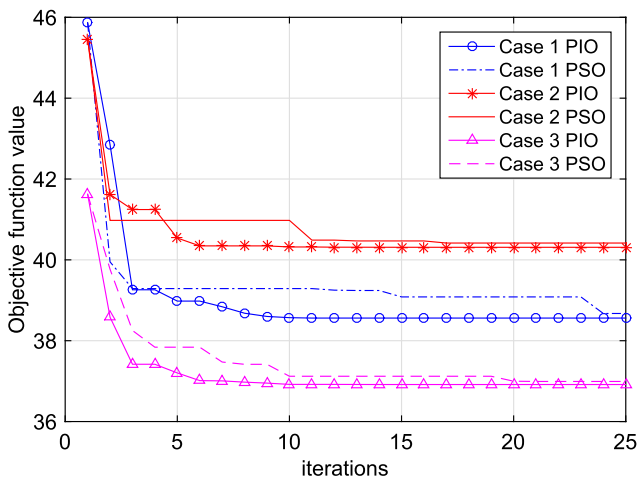
Table 6
Statistical performance comparison of PIO and PSO algorithms with 10 runs for cases 1, 2 and 3.

Cases	Algorithm	Iterations		J	
		μ	σ	μ	σ
Case 1	PIO	13	1.8738	38.5655	0.0101
	PSO	19	7.102	39.9242	0.6447
Case 2	PIO	14	3.0203	40.3266	0.0129
	PSO	20	4.1865	40.4757	0.3474
Case 3	PIO	13	0.9661	36.9075	0.0013
	PSO	19	6.3953	37.0313	0.1

5.1. Advantages of PIO over PSO

- The map and compass operator of PIO algorithm has an exponential weighting factor e^{-Rk} associated with the previous velocity of pigeons as given in Eq. (29), whereas, PSO has a weight w which is either constant or linearly varying in the velocity update equation. With the increase in the number of iterations, this weighing factor in PIO reduces the influence of pigeons previous velocity on the current velocity and allows PIO algorithm to converge at a faster rate to the optimal value than PSO algorithm.
- Update of pigeons position in the landmark operator of PIO algorithm is performed by considering the fitness values of each pigeon, while PSO algorithm doesn't consider the quality of its particles.
- The update equations of PSO algorithm requires usage of the best position that the particle has achieved so far. Therefore, it requires memory, while PIO algorithm is independent of this aspect.

Fig. 6 shows the bank angle profile for all the cases. The bank angle magnitude is zero in all the cases till the vehicle attains the sufficient dynamic pressure. There is a sudden decrease in the magnitude of the bank angle after the initial descent in all the cases. This leads to an increase in the vertical component of lift resulting in pull up as evidenced in Fig. 9. Subsequently, the magnitude of bank angle increases gradually bringing the vehicle into the denser atmosphere.

In all the cases, bank angle required to fly at QEGC is used for integrating the equations of motion until the load factor constraint becomes active. As soon as the load factor constraint is violated, bank angle obtained from Eq. (50) is

Fig. 5. The best objective function value corresponding to each iteration of PIO and PSO for cases 1, 2 and 3.
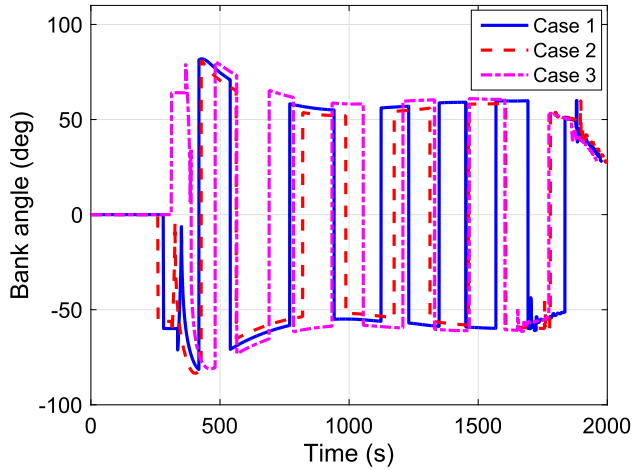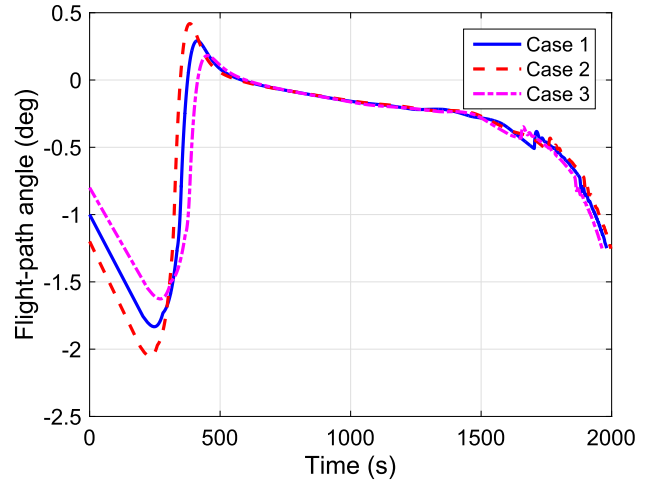
Fig. 6. Bank angle profiles.

Fig. 8. Variation of flight-path angle with time.

used to make the vehicle fly at altitude obtained from the load factor limits. Therefore, the magnitude of bank angle oscillates to satisfy load factor constraint. It is clear from Fig. 13 that load factor constraint of 1.65 g are accurately met in all the cases. The sign of bank angle changes based on the heading error corridor. There is a corresponding change in heading direction with each zero crossing of the bank angle. The angle of attack profile corresponding to obtained α_{pio} and m_{pio} is shown in Fig. 7. At higher Mach numbers, angle of attack is high so as to minimizes the peak heat rate and subsequently, its magnitude reduces.

The flight-path angle variation is seen in Fig. 8. It is seen that the commanded bank angle required to track the reference altitude rate dr_a/de, increases the flight-path angle whenever the load factor constraint becomes active. From the altitude variation plot in Fig. 9, it is observed that the vehicle satisfies QEGC in all the cases. The oscillations in the altitude profiles observed in the results section of Sushnigdha and Joshi (2017) are eliminated.

The ground track of the vehicle is given in Fig. 12. With series of bank reversals, the vehicle tries to travel along the
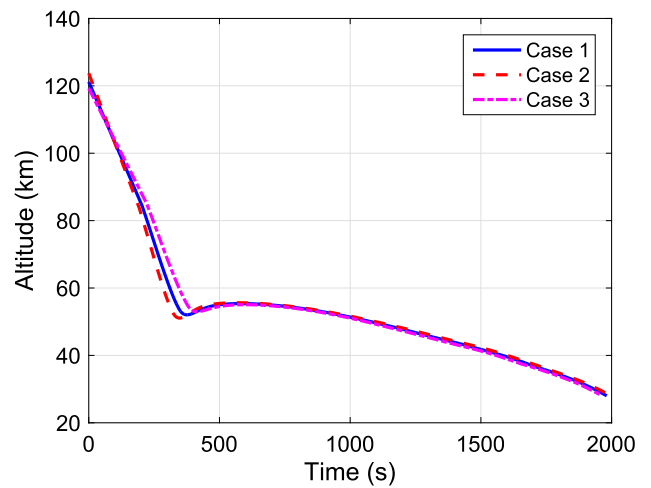
Fig. 9. Variation of altitude with time.
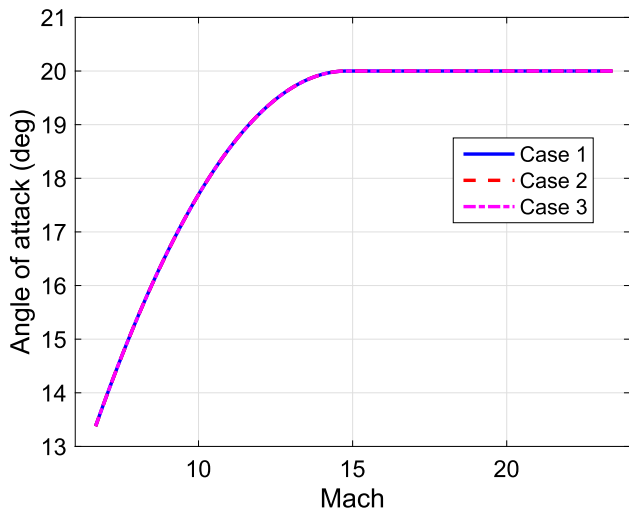
Fig. 10. Variation of velocity with time.

Fig. 7. Angle of attack profile.

great circle arc connecting the entry interface to the destination. The terminal velocity of 2000 m/s and range-to-go of 92 km are achieved as seen in Figs. 10 and 11
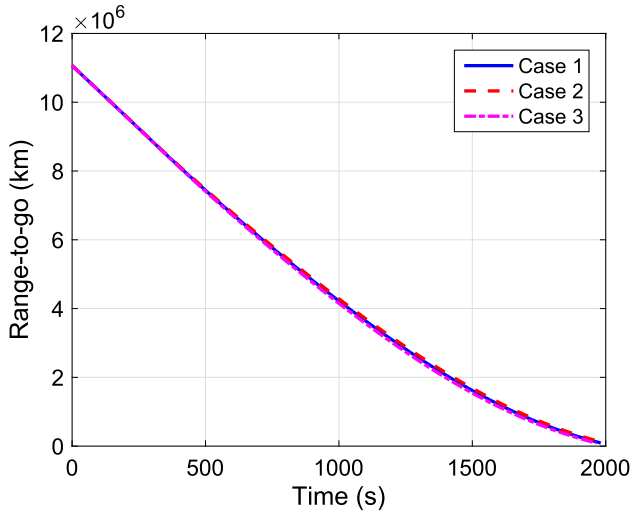
Fig. 11. Variation of range-to-go with time.
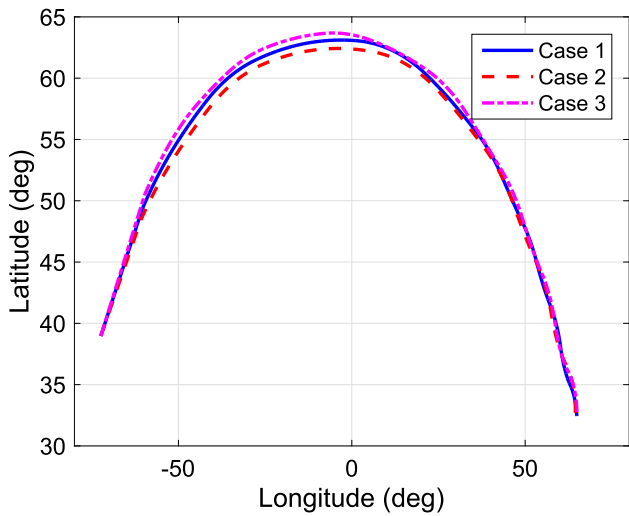
Fig. 12. Ground track.
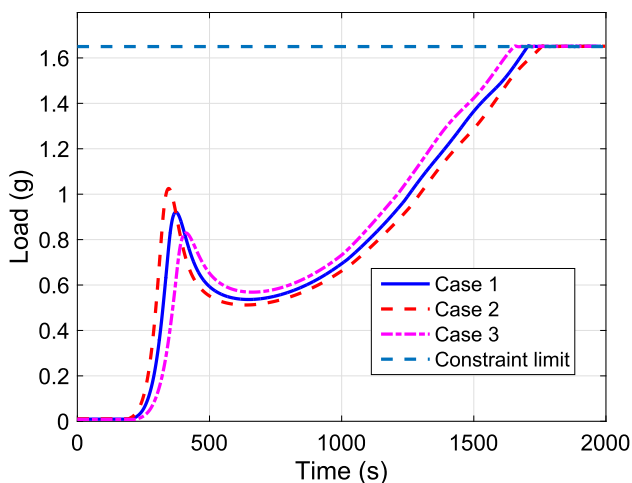
respectively. As the initial flight-path angle is higher in case 2, the minimum peak heat rate experienced by the vehicle is higher compared to other cases as seen in Fig. 14. The dynamic pressure variation with time is shown in Fig. 15.

5.2. Bank reversals

The philosophy behind bank reversals is to make sure that crossrange is within the predefined limits. Whenever crossrange exceeds the predefined tolerance, bank angle is commanded to reverse its sign. If the predefined tolerance is small, then the number of bank reversals are more. Similarly, when the tolerance is large, the number of bank reversals are less. Lesser number of bank reversals are applicable if larger crossrange errors are allowed to build up. Moreover, larger crossrange errors lead to large terminal errors in latitude and longitude. For this reason, a tighter tolerance limit of crossrange is chosen in the simulations to ensure that terminal conditions on latitude and longitude are met. As a consequence, larger number of bank reversals are inevitable.

To show the implication of number of bank reversals, case 1 given in Table 1 is considered. Case 1 is simulated with 6 and 11 bank reversals respectively. As seen in Fig. 16, crossrange errors are less when more bank reversals are present and the achieved terminal latitude and longitude are 32.42°, 65.49° respectively. The crossrange errors are more when the number of bank reversals are less and the achieved terminal latitude and longitude are 32.39°, 63.68° respectively. The latitude and longitude of the destination site being 31.6° and 65.7°, the terminal errors in latitude and longitude are larger in the case with fewer bank reversals. Therefore, more bank reversals are considered to reduce the crossrange and terminal errors in latitude and longitude. The ground track for both the cases along with great circle arc connecting the entry point and landing-site is shown in Fig. 17.

Fig. 13. Variation of load factor with time.
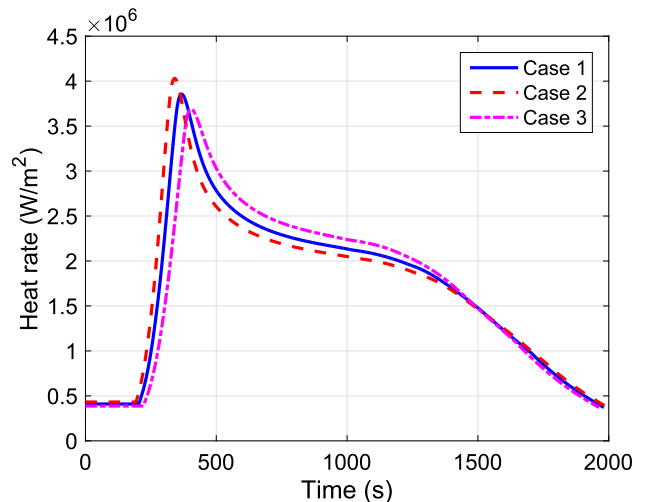
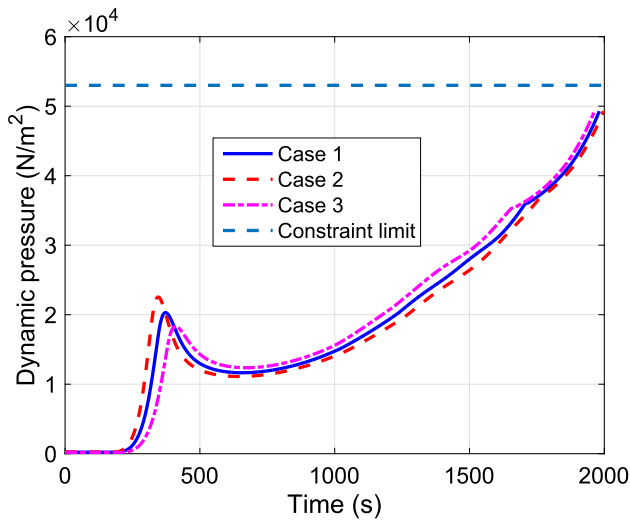Fig. 14. Heat rate variation with time.
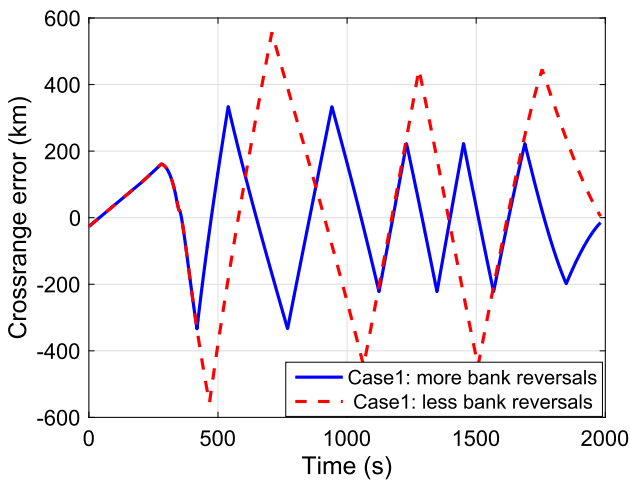
Fig. 15. Variation of dynamic pressure.
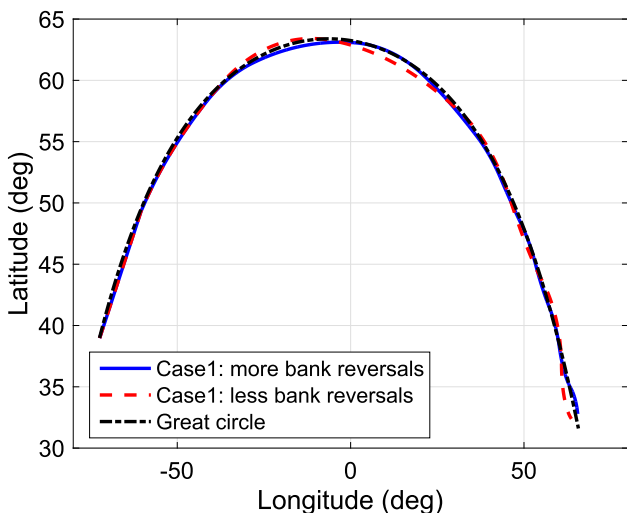

Fig. 16. Variation of crossrange.

Fig. 17. Ground track in comparison with great circle.

5.3. Sub-cases

Five sub-cases along with different load factor limits and entry conditions are discussed in Table 7. Entry conditions are same as the previous cases. These sub-cases are considered to show the effectiveness of the proposed schemes. The dimension of the problem is now reduced to one as the bank angle σ_0 is the control variable to be found, with the nominal angle of attack profile obtained in the corresponding previous cases. Sub-cases 4 and 5 are to test the robustness of the proposed methodologies in the presence of parametric dispersions. Uncertainties of $+25\%$ in density, $+10\%$ in C_L, $+10\%$ in C_D and $+5\%$ in mass of the vehicle are introduced in sub-case 4. Uncertainties of -25% in density, -10% in C_L, -10% in C_D and -5% in mass of the vehicle are introduced in sub-case 5. These uncertainties are considered according to Joshi et al. (2007) and are held constant throughout the simulations. The bank angle profiles obtained in these sub-cases are shown in Fig. 18. The bank angle σ_0 obtained using PIO algorithm for sub-cases are $61.165°, 56.47°, 63.958°, 55.81°, 64.53°$ respectively. In the initial phase, magnitude of bank angle decreases to make the vehicle fly at higher altitude. Thereafter magnitude of bank angle increases, leading the vehicle to denser atmosphere. This modulation of bank angle is required to eliminate the oscillations and satisfy QEGC. Towards the end of reentry phase, bank angle is modulated to satisfy the load factor constraint.

The entry profile corresponding to sub-case 1 along with the entry corridor formed by the constraint limits is shown in Fig. 19. It is clear from Fig. 19, that the entry profile lies within the entry corridor. It is also observed that the constraint on dynamic pressure is implicitly satisfied when the vehicle flies at altitudes higher than the altitude limit corresponding to load factor constraint limit. Therefore, the constraint on dynamic pressure is not explicitly considered in this paper. However, the same logic that modulates the bank angle command using Eq. (50) can be used whenever the dynamic pressure constraint is violated.

It can be seen from Fig. 21, that the load factor constraints in sub-cases are satisfied. The altitude profile of entry trajectory doesn't exhibit oscillations as seen in Fig. 20. An acceptable maximum terminal altitude error of about 1.5 km is observed in some of these sub-cases.

Table 7
Details regarding initial conditions and load factor limits for sub-cases.

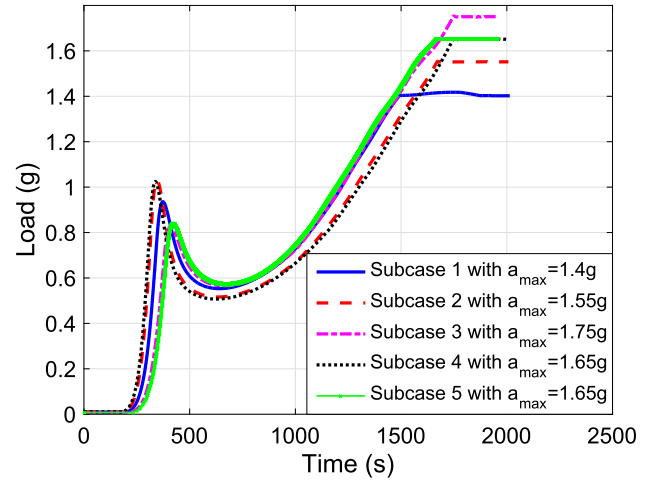| Sub-cases	Initial conditions	a_{max}
1	Case 1	1.4 g
2	Case 2	1.55 g
3	Case 3	1.75 g
4	Case 2	1.65 g
5	Case 3	1.65 g
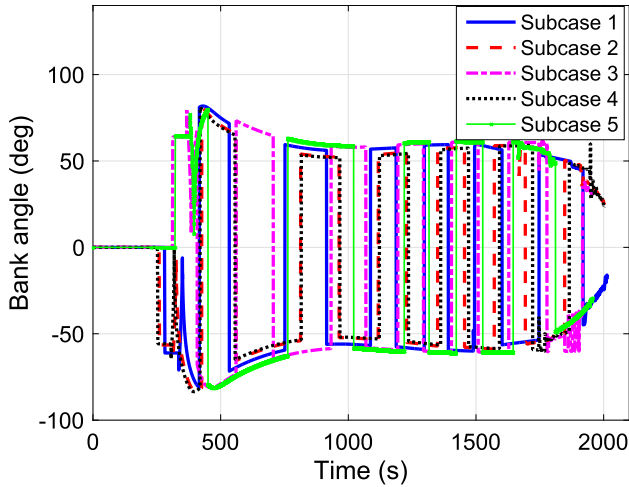
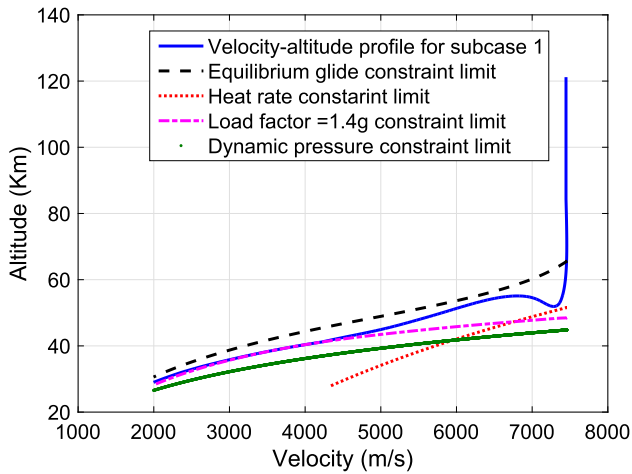Fig. 18. Bank angle profile for various subcases.

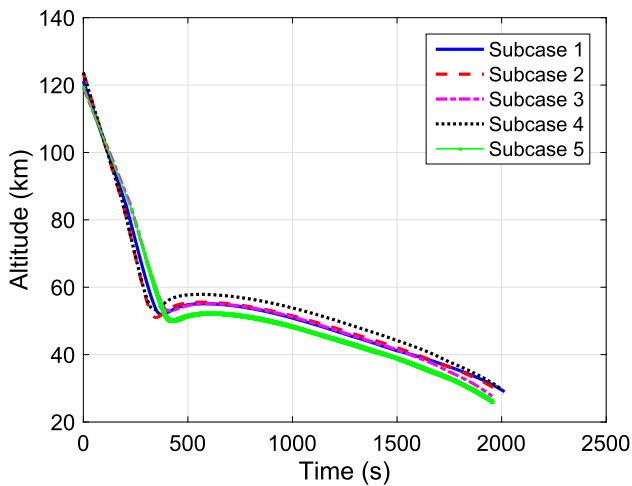Fig. 19. Entry profile within the corridor.

Fig. 20. Variation of altitude with time for subcases.

5.4. Sub-cases to test the robustness

Further, the following cases in Table 8 are considered to show the robustness of the proposed strategies towards

Fig. 21. Variation of load factor for different subcases.

parameter dispersions. Initial conditions for Case 2 given in Table 1 are considered and dispersions in coefficient of drag, lift, atmospheric density and mass are introduced. The angle of attack profile obtained from case 2 is considered as nominal control profile and bank angle σ_0 is obtained using PIO algorithm to minimize objective function given in Eq. (26). Load factor constraint is the same as that of case 2. The considered parametric dispersion ranges are in accordance with Joshi et al. (2007).

In the presence of the above parametric dispersions, the proposed scheme has eliminated the oscillations in the altitude profile as shown in Fig. 22. The entry trajectory has also satisfied the load factor constraint accurately in all the cases as seen in Fig. 23. The bank angle profile obtained using PIO algorithm follows same trend as the previous cases. The angle of attack profile is same as that of the case 2. The presence of parametric dispersions has resulted in terminal altitude errors of 1.3 km, 0.3 km, 0.7 km, 1.2 km, and 1.5 km in cases S1, S2, S3, S4 and S5 respectively. These terminal errors are within the acceptable tolerance limits. The terminal errors in velocities and range-to-go are very small. The dispersions in final positions around the landing site in all the cases and subcases considered so far are shown in Fig. 24. The achieved terminal positions are within the allowable tolerance limit.

5.5. Cases to test the applicability

The applicability of proposed strategies that eliminate entry trajectory oscillations and satisfy load factor constraint is tested by considering 5 cases with different latitude

Table 8
Dispersions in parameters for Case 2.

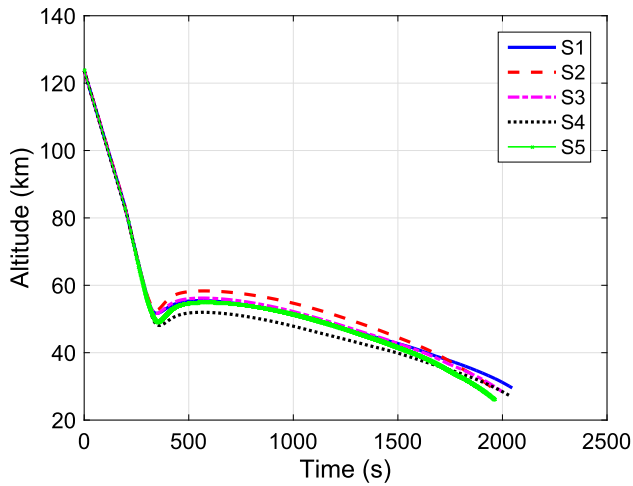| Cases	δC_L	δC_D	$\delta \rho$	δm
S1	+10%	−10%	+25%	+5%
S2	−10%	+10%	+25%	+5%
S3	−10%	−10%	+25%	+5%
S4	+10%	−10%	−25%	−5%
S5	−10%	+10%	−25%	−5%

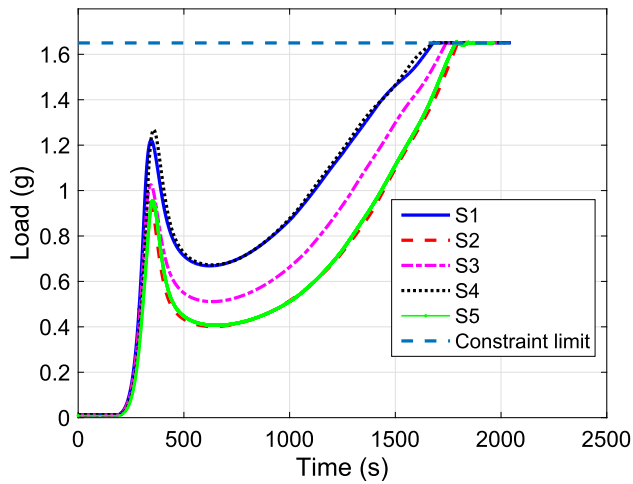Fig. 22. Variation of altitude under parameter dispersions.

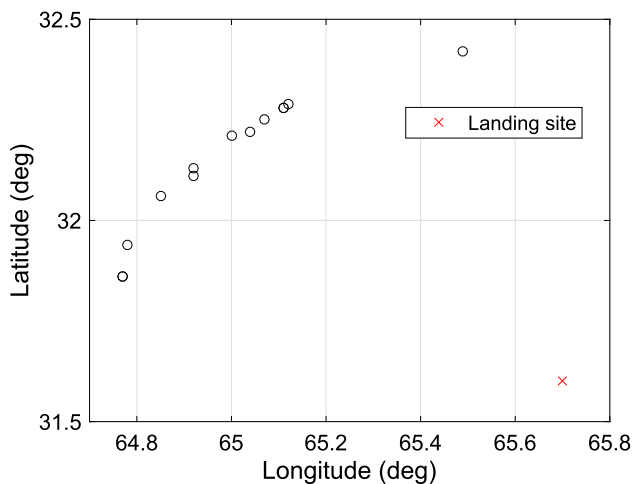Fig. 23. Variation of load factor under parameter dispersions.

Fig. 24. Final dispersions around the landing site.

and longitude of entry interface and different destinations. Entry conditions in altitude, velocity, flight-path angle are same as case 2 given in Table 1. Desired terminal conditions in altitude, range-to-go, and velocity are same as given in Table 2. The details of entry conditions and destinations are given in Table 9.

The control variables are bank angle and angle of attack that are found using PIO algorithm. The objective function is given in Eq. (25). The bank angle profiles corresponding to each case is shown in Fig. 25. The same trend in bank

Table 9
Latitude and longitude at the entry interface and destination.

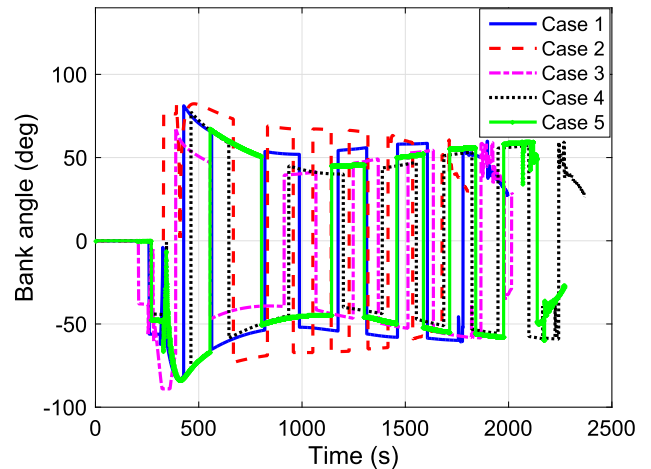| Cases	θ_0 (deg)	ϕ_0 (deg)	ψ_0 (deg)	s_0 (km)	θ^* (deg)	ϕ^* (deg)
1	−72.42	38.99	37	11,112	65.7	31.6
2	180	35	90	10,206	265	−10
3	0	50	−10	11,009	−165	30
4	0	50	120	13,303	90	−40
5	0	50	60	12,735	130	0

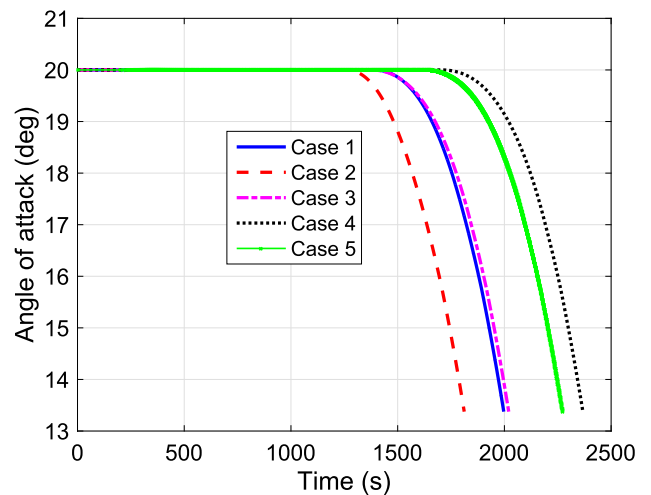Fig. 25. Bank angle profiles for different cases.
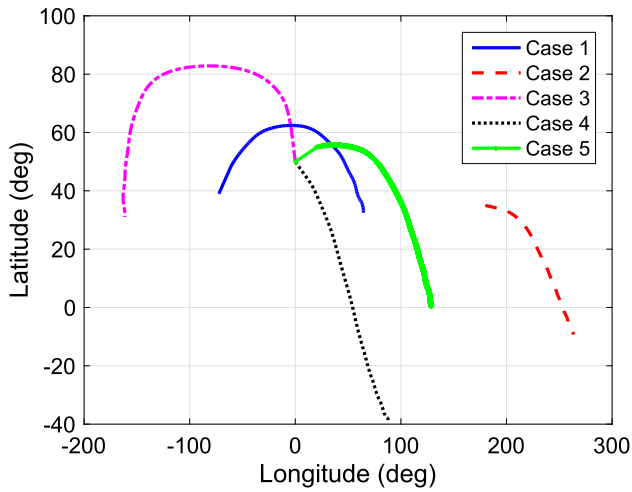

Fig. 26. Angle of attack variation with time.

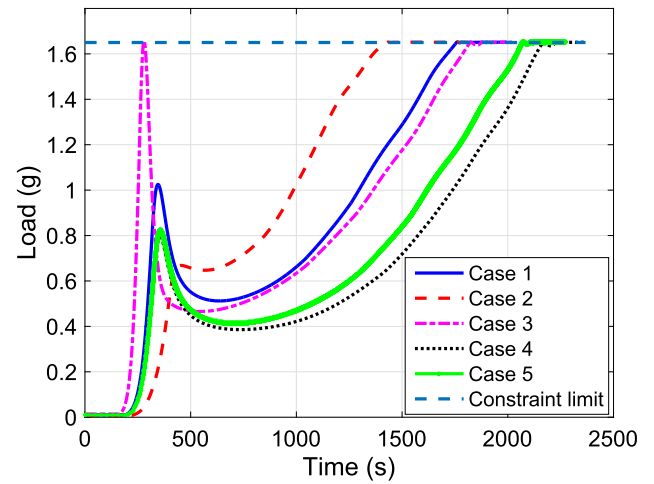Fig. 27. Ground track for different cases.
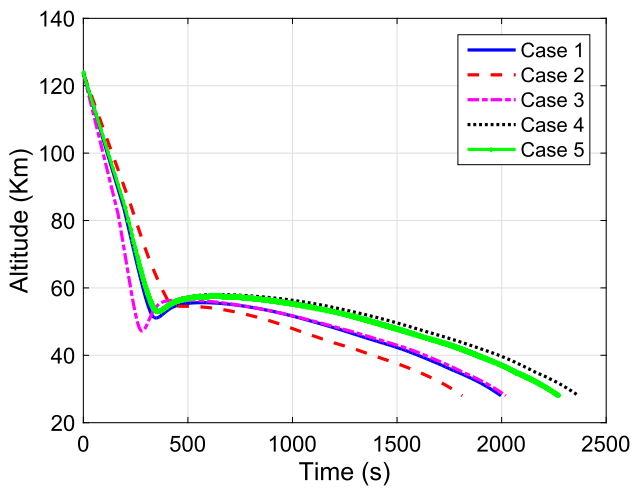

Fig. 30. Variation of load factor.
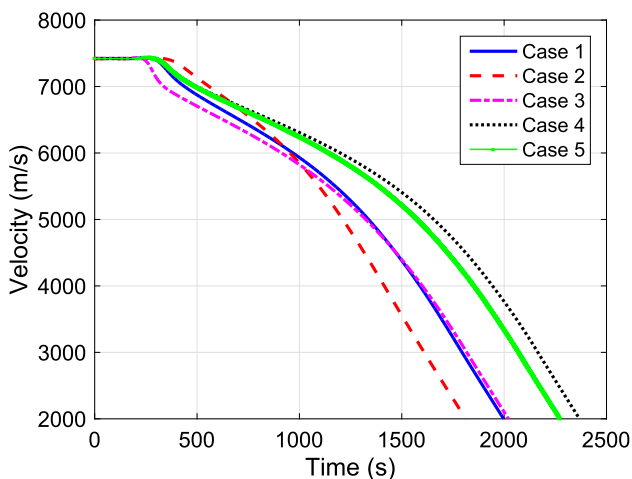

Fig. 28. Altitude profiles.

Fig. 29. Variation of velocity.

angle is observed to satisfy QEGC and load factor constraint. The angle of attack profile is given in Fig. 26. The ground track of these cases is shown in Fig. 27. It is seen that the entry trajectory satisfies the required terminal range-to-go, altitude, and velocity. The altitude profile is shown in Fig. 28. It is clear that the vehicle satisfies QEGC. The velocity and load factor variations are given in Figs. 29 and 30 respectively. Load factor constraint is satisfied in all the 5 cases. It can be concluded that the proposed methodology for satisfying QEGC and load factor constraints as part of PIO algorithm is applicable to various re-entry missions.

6. Conclusion

In this paper, the entry trajectory optimization problem is solved using PIO algorithm to obtain the control profiles that minimize the peak heat rate, satisfy terminal conditions, equilibrium glide condition and various load factor constraints. Three cases with slightly dispersed initial entry conditions and parameter uncertainties are considered to show the robustness of the proposed schemes. To ensure applicability of the proposed schemes, 5 cases with different entry locations and destinations are presented. The entry trajectory derived from the control profiles obtained using PIO algorithm has minimized the peak heat rate experienced by the vehicle in the initial descent phase and has satisfied the terminal error constraints accurately. In these cases where the dimension of the problem is three, PIO algorithm has converged in less number of iterations compared to PSO algorithm. The angle of attack profile obtained in these cases suggest that the high angle of attack is required at higher Mach numbers to minimize the peak heat rate and subsequently after reaching a particular Mach number its magnitude should slowly decrease to satisfy the desired terminal altitude. This angle of attack profile is considered to be the nominal angle of attack profile for the remaining sub-cases, where bank angle alone is modulated to satisfy the desired load factor constraint.

The proposed schemes for incorporating QEGC and load factor constraints are very simple. They utilize the slope of altitude limits of path constraints in the altitude-velocity space and from the simulation results it is seen that the proposed methodology has successfully constrained load factor to 1.4 g, 1.55 g and 1.75 g in three different sub-cases. The simulation results of all the cases have satisfied QEGC, path constraints, and terminal conditions.

Acknowledgements

References

Anon, 1976. U.S. Standard Atmosphere. U.S. Committee on Extension to the Standard Atmosphere, Washington, D.C.

Bailing, T., Qun, Z., 2011. Optimal guidance for reentry vehicles based on indirect legendre pseudospectral method. Acta Astronaut. 68 (7), 1176–1184. https://doi.org/10.1016/j.actaastro.2010.10.010.

Betts, J., 2001. Practical Methods for Optimal Control Using Nonlinear Programming. Society for Industrial and Applied Mathematics Press.

Cai, W.W., Zhu, Y.W., Yang, L.P., Zhang, Y.W., 2015. Optimal guidance for hypersonic reentry using inversion and receding horizon control. IET Control Theory Appl. 9 (9), 1347–1355.

Deng, Y., Duan, H., 2016. Control parameter design for automatic carrier landing system via pigeon-inspired optimization. Nonlinear Dyn. 85 (1), 97–106.

Duan, H., Qjao, P., 2014. Pigeon-inspired optimization: a new swarm intelligence optimizer for air robot path planning. Int. J. Intell. Comput. Cybernet. 7 (1), 24–37. https://doi.org/10.1108/IJICC-02-2014-0005.

Duan, H., Wang, X., 2016. Echo state networks with orthogonal pigeon-inspired optimization for image restoration. IEEE Trans. Neural Networks Learn. Syst. 27 (11), 2413–2425.

Joshi, A., Sivan, K., Amma, S.S., 2007. Predictor-corrector reentry guidance algorithm with path constraints for atmospheric entry vehicles. J. Guid., Control, Dyn. 30 (5), 1307–1318.

Li, C., Duan, H., 2014. Target detection approach for uavs via improved pigeon-inspired optimization and edge potential function. Aerosp. Sci. Technol. 39, 352–360. https://doi.org/10.1016/j.ast.2014.10.007.

Lu, P., 2006. Asymptotic analysis of quasi-equilibrium glide in lifting entry flight. J. Guid., Control, Dyn. 29 (3), 662–670. https://doi.org/10.2514/1.15789.

Lu, P., 2014. Entry guidance: a unified method. J. Guid., Control, Dyn. 37 (3), 713–728. https://doi.org/10.2514/1.62605.

Phillips, T.H., 2003. A Common Aero Vehicle (CAV) Model, Description, and Employment Guide. Schafer Corp. for Air Force Research Laboratory and Air Force Space Command.

Pontryagin, L., Boltyanskii, V., 1987. The Mathematical Theory of Optimal Processes. Wiley Interscience, New York.

Qiu, H., Duan, H., 2015. Multi-objective pigeon-inspired optimization for brushless direct current motor parameter design. Sci. China Technol. Sci. 58 (11), 1915–1923.

Rahimi, A., Dev Kumar, K., Alighanbari, H., 2013. Particle swarm optimization applied to spacecraft reentry trajectory. J. Guid., Control, Dyn. 36 (1), 307–310. https://doi.org/10.2514/1.56387.

Shen, Z., Lu, P., 2004. Dynamic lateral entry guidance logic. J. Guid., Control, Dyn. 27 (6), 949–959. https://doi.org/10.2514/1.8008.

Sushnigdha, G., Joshi, A., 2017. Re-entry trajectory design using pigeon inspired optimization. In: AIAA Atmospheric Flight Mechanics Conference. AIAA, Denver, Colorado, pp. 1–12.

Wu, J., Wang, H., Li, N., Yao, P., Huang, Y., Su, Z., Yu, Y., 2017. Distributed trajectory optimization for multiple solar-powered uavs target tracking in urban environment by adaptive grasshopper optimization algorithm. Aerosp. Sci. Technol. 70, 497–510.

Wu, J., Wang, H., Li, N., Yao, P., Huang, Y., Yang, H., 2018. Path planning for solar-powered uav in urban environment. Neurocomputing 275, 2055–2065.

Xue, Q., Duan, H., 2017. Robust attitude control for reusable launch vehicles based on fractional calculus and pigeon-inspired optimization. IEEE/CAA J. Automat. Sinica 4 (1), 89–97.

Yu, Y., Wang, H., Li, N., Su, Z., Wu, J., 2017. Automatic carrier landing system based on active disturbance rejection control with a novel parameters optimizer. Aerosp. Sci. Technol. 69, 149–160.

Zhang, B., Duan, H., 2017. Three-dimensional path planning for uninhabited combat aerial vehicle based on predator-prey pigeon-inspired optimization in dynamic environment. IEEE/ACM Trans. Comput. Biol. Bioinf. 14 (1), 97–107.

Zhao, J., Zhou, R., 2015a. Particle swarm optimization applied to hypersonic reentry trajectories. Chin. J. Aeronaut. 28 (3), 822–831. https://doi.org/10.1016/j.cja.2015.04.007.

Zhao, J., Zhou, R., 2015b. Pigeon-inspired optimization applied to constrained gliding trajectories. Nonlinear Dyn. 82 (4), 1781–1795. https://doi.org/10.1007/s11071-015-2277-9.